

UCLA

UCLA Previously Published Works

Title

Functional Genomics Approach Identifies Novel Signaling Regulators of TGF α Ectodomain Shedding

Permalink

<https://escholarship.org/uc/item/77d7g2qk>

Journal

Molecular Cancer Research, 16(1)

ISSN

1541-7786

Authors

Wilson, Jennifer L
Kefaloyianni, Eirini
Stopfer, Lauren
[et al.](#)

Publication Date

2018

DOI

10.1158/1541-7786.mcr-17-0140

Peer reviewed

Functional Genomics Approach Identifies Novel Signaling Regulators of TGF α Ectodomain Shedding

Jennifer L. Wilson¹, Eirini Kefaloyianni², Lauren Stopfer¹, Christina Harrison³, Venkata S. Sabbiseti⁴, Ernest Fraenkel^{1,5}, Douglas A. Lauffenburger¹, and Andreas Herrlich²



Abstract

Ectodomain shedding of cell-surface precursor proteins by metalloproteases generates important cellular signaling molecules. Of importance for disease is the release of ligands that activate the EGFR, such as TGF α , which is mostly carried out by ADAM17 [a member of the A-disintegrin and metalloprotease (ADAM) domain family]. EGFR ligand shedding has been linked to many diseases, in particular cancer development, growth and metastasis, as well as resistance to cancer therapeutics. Excessive EGFR ligand release can outcompete therapeutic EGFR inhibition or the inhibition of other growth factor pathways by providing bypass signaling via EGFR activation. Drugging metalloproteases directly have failed clinically because it indiscriminately affected shedding of numerous substrates. It is therefore essential to identify regulators for EGFR ligand cleavage. Here, integration of a functional

shRNA genomic screen, computational network analysis, and dedicated validation tests succeeded in identifying several key signaling pathways as novel regulators of TGF α shedding in cancer cells. Most notably, a cluster of genes with NF κ B pathway regulatory functions was found to strongly influence TGF α release, albeit independent of their NF κ B regulatory functions. Inflammatory regulators thus also govern cancer cell growth-promoting ectodomain cleavage, lending mechanistic understanding to the well-known connection between inflammation and cancer.

Implications: Using genomic screens and network analysis, this study defines targets that regulate ectodomain shedding and suggests new treatment opportunities for EGFR-driven cancers. *Mol Cancer Res*; 16(1): 147–61. ©2017 AACR.

Introduction

EGFR activation generates signals for cell proliferation, migration, differentiation, or survival (reviewed in ref. 1), cellular phenotypes that are often dysregulated in cancer. A-disintegrin-and-metalloprotease-17 (ADAM17) releases most ligands that activate the EGFR, for example, TGF α (2–4). ADAM17, EGFR ligands, and EGFR are indeed upregulated in numerous different cancer types, driving EGFR activity that promotes cancer growth and metastasis (reviewed in refs. 1 and 5). The same components, ADAM17 and EGFR/EGFR ligands, have also been associated, for example, with the development of organ fibrosis in lung,

liver, or kidney (6–9) and have important roles in inflammation (reviewed in refs. 10, 11). Broad-spectrum metalloprotease inhibition has been unsuccessful in the clinic due to significant side effects resulting from indiscriminate suppression of the cleavage of many metalloprotease substrates and their dependent physiologic functions (reviewed in refs. 12, 13). Even recently developed selective ADAM10 or 17 inhibitors still affect the cleavage of many substrates (14, 15). Existing strategies to target EGFR itself would be more specific, but they also have had limited therapeutic success in cancer and other disease applications due to development of resistance to the inhibitors (16, 17).

Excessive release of EGFR ligands is an important mechanism of therapeutic resistance in cancer treatment. It can outcompete attempts to block ligand binding to EGFR or to block EGFR kinase activity (18–20), and it can confer resistance to inhibition of other oncogenic driver pathways by establishing "bypass signaling" via the EGFR pathway (21). As examples for the latter, EGF can induce resistance to cMet inhibition (crizotinib) in lung cancer patients (22, 23), EGF or NRG1 can induce resistance to cMet inhibition in cMet-amplified gastric cancer cells and BRAF (V600E) inhibition in melanoma cells (21), and TGF α causes resistance to ALK inhibition in lung cancer cells (24). Development of strategies to target EGFR ligand release is therefore of great importance for successful inhibition of the EGFR pathway and for effective targeting of other growth pathways under current clinical investigation in cancer and other diseases.

Ectodomain shedding by ADAMs can be induced by activation of intracellular signaling pathways involving, for example,

¹Department of Biological Engineering, Massachusetts Institute of Technology, Cambridge, Massachusetts. ²Division of Nephrology, Washington University School of Medicine, St. Louis, Missouri. ³Department of Biology, University of Massachusetts, Boston, Massachusetts. ⁴Renal Division, Brigham and Women's Hospital, Boston, Massachusetts. ⁵Department of Biology, Massachusetts Institute of Technology, Cambridge, Massachusetts.

Note: Supplementary data for this article are available at Molecular Cancer Research Online (<http://mcr.aacrjournals.org/>).

Corresponding Authors: Andreas Herrlich, Washington University School of Medicine, 660 South Euclid Avenue, Wohl Clinic Rm 9934, St. Louis, MO 63108. Phone: 314-747-0565; Fax: 314-362-8237; E-mail: aherrlich@wustl.edu; and Douglas Lauffenburger, Massachusetts Institute of Technology, 77 Massachusetts Ave, 16-343, Cambridge, MA 02139. Phone: 617-252-1629; E-mail: lauffen@mit.edu

doi: 10.1158/1541-7786.MCR-17-0140

©2017 American Association for Cancer Research.

Wilson et al.

calcium influx, the activation of G-protein-coupled receptors, and the release of diacylglycerol, an activator of protein kinase C (PKC; ref. 25). Several mechanisms that regulate cleavage on the level of ADAM17 have been reported, including regulation of expression, maturation, trafficking to the cell surface (reviewed in ref. 12), posttranslational modifications of ADAM17's ectodomain (26–29) or C-terminus (by the MAPKs p38 or ERK; refs. 30, 31), and interaction with other transmembrane proteins, such as iRhom1/2 (32, 33) and annexins (34, 35). In addition, a small domain contained in the ectodomain of ADAM17 has been identified that interacts with and regulates the cleavage of a small subset of ADAM17 substrates (36, 37). Specific regulation of substrate cleavage also involves intracellular signal-induced C-terminal modifications of the substrate (4, 25, 38, 39) that lead to protease accessibility changes of the substrate's ectodomain (40), but it has remained mostly unknown which intracellular signaling components and pathways are involved (reviewed in ref. 12).

To identify such signaling components and pathways that regulate induced TGF α cleavage, we carried out an shRNA screen of all human kinases and phosphatases. An early limited screen analysis revealed that protein-kinase-C- α PKC α and the PKC-regulated protein-phosphatase-1-inhibitor-14D (PPP1R14D) are required for specific regulation of phorbol ester (TPA; a diacylglycerol mimic and PKC activator)- or angiotensin II-induced shedding of TGF α and that this regulation indeed occurred on the substrate and not the protease level (4).

Here we report a combined experimental and computational approach for discovering novel regulators of TGF α cleavage. First, using stringent analysis of our primary shRNA screen carried out in acute T-cell leukemia-derived Jurkat cells, we validated a significant number of positive and negative regulators of TGF α cleavage in triple-negative breast cancer cells. We then modeled and validated signaling pathways identified in an integrative network modeling approach. This network incorporated experimental genes measured in the screen and predicted genes that regulate TGF α cleavage in different cancer cells. We discovered and validated a cluster of TGF α -regulatory genes that are also known to influence NF κ B signaling and show that NF κ B-regulatory functions of these proteins are not required for their cleavage-regulatory functions.

Our results thus define targets that might allow therapeutic control of EGFR ligand ectodomain shedding and thus avoid EGFR ligand-mediated therapeutic resistance. More broadly, our results highlight quite generally how a network approach can improve shRNA screen validation, provide new opportunities for existing therapies, and identify genes relevant for EGFR-driven diseases.

Materials and Methods

The initial screen was conducted in Jurkat cells, as is fully described in ref. 4. An important feature of this screen is that it uses a Jurkat-TE cell line which expresses TGF α with an intracellular GFP and extracellular HA tag.

shEnrich method

The shEnrich method analyzes redundant shRNAs against a given gene to select for consistency and strength of biological effect (in our case, projected effect on TGF α shedding). The method rank-orders all shRNAs and calculates a moving enrichment score (ES) based on summing the probability of finding an

shRNA within the gene's family (probability of a hit, "p_hit") and the probability of finding an shRNA outside the family (probability of a miss, "p_miss"). For each gene's shRNA cohort, there is a total effect represented by the sum of all shRNAs z-scores; the p_hit is a fractional representation of how much of this total effect is captured at each rank. The p_miss is a fractional penalty equivalent to the inverse of the number of nonfamily shRNAs in the screen.

A phosphorylation site-specific interactome

We used the set of human interactions contained in version 13 of the iRefIndex database (41) as our source for protein-protein interactions, which consolidates information from a variety of source databases. We used the MIscore system (42) to assign confidence scores (ranging from 0 to 1) to these interactions; this scoring system considers the number of publications (publication score), the type of interaction (type score), and the experimental method used to find the interaction (method score). We extracted the relevant scoring information for interactions from the iRefIndex MITAB2.6 file, using the redundant interaction group identifier (RIGID) to consolidate interactions between the same two proteins reported by multiple databases, and used a java implementation of MIscore (version 1.3.2, available at <https://github.com/EBI-IntAct/miscore/blob/wiki/api.md>) with default parameters for individual score weights. We only considered interactions between two human proteins (i.e., we excluded human-viral interactions) and converted protein identifiers, generally provided as UniProt or RefSeq accessions, to valid HUGO gene nomenclature committee (HGNC) symbols. Once converted, we removed redundant interactions (generally arising from isoform-specific interactions that map to the same protein/gene symbols) and retained the maximum observed score. This produced a total of 175,854 unique protein-protein interactions.

To this interaction set, we added predicted and experimental interactions for kinase and phosphatase sites. We collected the kinase-site interactions from Phosphosite (43) and phosphatase-site interactions from DEPOD (44, 45) Where site-specific information existed, we created edges in the interactome, first from the kinase/phosphatase to a substrate-site node (represented in the network as "PROTEIN_SITE") and second from the substrate-site to the substrate (represented as "PROTEIN"). The kinase/phosphatase to substrate-site interactions were scored using a modified MIscore framework (42). This scoring method is a normalized, weighted sum of an interaction type score (S_P), evidence type score (S_t), and publication value score (S_p):

$$S = \frac{K_p S_P + K_m S_m + K_t S_t}{K_p + K_m + K_t}$$

Using the MIscore framework as a guide, all interaction type scores (S_t) were set to 1 (because this interaction information was "direct"). Publication scores were set using the MIscore scale ($S_p = 0.00/0.33/0.53/0.67/0.77/0.86/0.94/1.00$ for 0/1/2/3/4/5/6/7 publications). The method scores (S_m) were set based on the evidence available for each dataset:

DEPOD	Phosphosite	
<i>in vitro</i> reaction or <i>in vivo</i> in one lab	0.33	<i>in vitro</i> evidence 0.33
<i>in vitro</i> and <i>in vivo</i> or evidence in multiple labs	0.66	<i>in vivo</i> evidence 0.66
<i>in vitro</i> and <i>in vivo</i> in multiple labs	1.0	both 1.0

All K values were set to 1. The interactome uses Uniprot identifiers. A text version of this interactome is hosted on the Fraenkel Lab website (<http://fraenkel-nsf.csbi.mit.edu/tgfshedding/>).

Prize-collecting Steiner Forest

We used the genes selected by the shEnrich method and the interactome network described above as inputs to the Prize-Collecting Steiner Forest algorithm (PCSF; ref. 46). The genes from shEnrich were all assigned prize values of 1 and converted to Uniprot identifiers. We used the parameters $\beta = 10$, $D = 10$, $\omega = 1$, and $\mu = 0.006$ (parameter optimization explained in Supplementary Methods). After finding an optimal network of genes, we augmented this forest and added back all possible interactions among these genes from our initial interactome. We converted to gene identifiers back to gene symbol and visualized the network in Cytoscape. The PCSF algorithm is available online as part of our "Omics Integrator suite of tools (<http://fraenkel-nsf.csbi.mit.edu/omicsintegrator/>)." An archived version of PCSF that was used for this analysis is hosted on the Fraenkel Lab website (<http://fraenkel-nsf.csbi.mit.edu/tgfshedding/>).

Sensitivity, specificity, and centrality metrics

To determine a gene's sensitivity within our network solution, we created a family of 100 networks using the original prize values and genes selected from the shEnrich method. In each of these simulations, we added 0.5% noise to the interaction edge scores in our interactome by randomly increasing or decreasing these edge scores by 0.5%. For a given gene, we measured sensitivity by counting the gene's representation in the family of noisy networks. A gene that shows up in all of the networks is insensitive to noise and thus robust to our method. Because the prize nodes are constant inputs to the algorithm, we expect them to be insensitive to edge noise. To measure specificity, we again created a family of 100 networks. This time, we hold the interactome constant and randomly select gene targets from our initial library as inputs. We run the algorithm at the same parameters as above and count a gene's representation in the family of random networks. We calculated $1 - \text{specificity}$ to rank genes that are specific to the real experimental data and eliminate biases in selection due to the initial library construction. For all centrality metrics, we used the networkX module in Python.

For aggregate scoring, we used the following equation to rank experimental and predicted genes:

$$W = \frac{(1 - \text{sens}) * \sigma_{\text{sens}} + (1 - \text{spec}) * \sigma_{\text{spec}} + \text{norm_cl} * \sigma_{\text{norm_cl}}}{\sigma_{\text{sens}} + \sigma_{\text{spec}} + \sigma_{\text{norm_cl}}}$$

In this equation, *sens*, *spec*, and *norm_cl* refer to a gene's sensitivity, specificity, and normalized closeness, and σ_{sens} , σ_{spec} , and $\sigma_{\text{norm_cl}}$ are the SDs of these measurements for the entire network.

Analysis of NF κ B-related cluster in model cell lines

We pulled RMA-normalized cell line expression data from CCLE (47) and plotted these values using the Seaborn package in Python.

Analysis of network-selected genes in cancer patient samples

We pulled patient mRNA expression data from www.cbioportal.org (RNA Seq. V2 RSEM, z-scores) for the time frame January

11, 2016 to February 11, 2016. The data for *IRAK1*, *CALM1*, *OBSCN*, *PPEF1*, and *PPEF2* across cancer types for histogram comparison was pulled from the same website on June 6, 2016. The data that were investigated were only from data using z-scores with a 0.0 threshold used for analysis (to have the data clearly represented without bias).

We further explored differential expression of human cancer cell lines using RNA-seq from EMBL expression Atlas (48). We selected for all instances of "cancer" versus respective "normal" tissue. We plotted the log₂ fold change expression as reported from the Expression Atlas Downloads and used Seaborn package in Python to group cancers based on their differential expression of NF κ B-related cluster genes. All differentially expressed genes are $P < 0.05$ using a *t* test provided by the Expression Atlas web interface.

Cell lines

Kato-III and MDA-MB-231 cells were purchased from ATCC in March, 2016. Both cells lines were tested for mycoplasma using the Lonza MycoAlert Mycoplasma Detection Kit. We tested cells within one month of arrival and expanded the initial population into aliquots for all further experiments.

shRNA knockdown experiments

MDA-MB-231 or Jurkat cells were transduced with lentiviral particles used in the original screen or, for newly identified regulators, obtained from Sigma Aldrich (Mission shRNA Transduction Particles). The clone IDs of the particles were: *PRKCA*: TRCN0000001693, TRCN0000001692; *PPP1R14D*: TRCN000000192, TRCN0000001924; *DUSP9*: TRCN0000002426, TRCN0000002427; *INPP5D*: TRCN00000039894, TRCN00000039896; *ENPP1*: TRCN0000002538, TRCN0000002537; *OBSCN*: TRCN00000021599, TRCN00000021602; *PPAP2A*: TRCN0000002579, TRCN0000002577; *PPEF1*: TRCN0000002551, TRCN0000002550; *PKIB*: TRCN0000002817, TRCN0000002815; *PPP4R1*: TRCN00000052763, TRCN00000052766; *PTPRE*: TRCN0000002893, TRCN0000002895; *SSH3*: TRCN0000002612, TRCN0000002613; *SH2D1A*: TRCN0000360148, TRCN0000367940 TRCN0000360149; *PTPN22*: TRCN0000355586, TRCN0000355534, TRCN0000355533; *TAB1*: TRCN0000381913, TRCN0000380746, TRCN0000380345; *XIAP*: TRCN0000231575, TRCN0000231576, TRCN0000231577. MDA-MB-231 or Jurkat cells were plated at 2.5×10^5 cells per well in 96-well plates, and infected with 1- μ L of virus in media with 4 μ g/mL polybrene. After 24 hours (day 1), cells were switched to media with of puromycin (2 μ g/mL or 2.5 μ g/mL for MDA-MB-231 or Jurkat cells, respectively). On day 3, fresh media with puromycin was added. On day 5, cells were switched to regular growth media and allowed to recover before stimulation. On day 7, cells were either stimulated with 100 nmol/L PMA or left in media. At 1 hour (MDA-MB-231, ELISA measurements) or 5 minutes (Jurkat, FACS analysis), released or surface-bound TGF α was measured.

Measuring surface-bound TGF α in Jurkat cells

For all measurements in Jurkat-TE cells, we used the following staining and washing procedure: Jurkat-TEs were spun out of media and resuspended in 25 μ L of 1:100 mouse anti-HA (Covance #MMS-101) on ice for 1 hour. Cells were washed three times with 200- μ L cold PBS with 3% FCS, and resuspended in 25- μ L 1:100 APC-coupled anti-mouse (BD Pharmingen #550826) on

Wilson et al.

ice for 2 hours. They were resuspended with propidium iodide (PI) and relative TGF α at the surface was quantified using FACS. We analyzed all FACS data using FlowJo. We measured the FITC and APC-A geometric means in the PI-negative (live) population. Relative TGF α is determined from the ratio of red:green fluorescence and represents the relative amounts of extracellular:intracellular TGF α .

Measuring TGF α shedding in Kato-III and MDA-MB-231 cell lines

Validation of screen hits was conducted using MDA-MB-231 cells plated in 96-well plates. Ninety-percent confluent cells were stimulated with 100 nmol/L PMA for 2 hours after which time supernatant was collected. A microsphere-based Luminex Technology and ELISA kits (DY239, R&D Systems) were used to measure a panel of shed growth factors, as described previously (49).

To measure changes in TGF α shedding with inhibitor treatments, 4×10^4 cells per well were plated in a 96-well plate, allowed to adhere overnight and then incubated with serum-free medium for 3 hours. Cells were then pretreated for 1 hour with DMSO control or IRAK4 inhibitor (5 μ mol/L AS2444697, TOCRIS) or IRAK1/4 inhibitor (5 μ mol/L IRAK1/4 Inhibitor I, TOCRIS) or IKK β inhibitor (2 μ mol/L BI605906, TOCRIS) or metalloprotease inhibitor (10 μ mol/L batimistat, TOCRIS) after which medium was replaced with fresh media containing the respective inhibitor and 100 nmol/L PMA (or vehicle). After 1-hour incubation, TGF α shedding in the cell culture medium was quantified using the DuoSet ELISA Development System (R&D Systems). Cell viability was immediately assessed using CellTiter-Glo Luminescent Cell Viability Assay (Promega).

TGF α shedding values (pg/mL) were normalized to cell viability measurements.

Statistical analysis

For Jurkat experiments, we conducted unpaired *t* tests using Prism software to assess significance. For all control shRNAs (denoted "shCtl" in each figure), $n = 6$ and for all other shRNAs, $n = 3$. In all cases, error bars are SEM. For the ELISA experiments in KATOIII or MDA-MB-231 cell lines, a one-way ANOVA test was performed using Prism software to determine significance of treatment conditions compared with the untreated control ($n = 5$). In all cases, error bars are SEM.

Results

A kinome/phosphatome screen for regulators of TGF α shedding

We conducted a screen for signaling regulators of TGF α shedding, comprising a library of 750 human kinases and phosphatases, using a FACS-based assay (Fig. 1A) in acute T-cell leukemia-derived Jurkat cells. Most genes were targeted by 4–5 redundant shRNAs (Fig. 1B). After gene knockdown, cells were stimulated for 2 minutes with phorbol ester (TPA), a commonly used cleavage stimulus that activates protein kinase C (PKC). We then measured mean geometric extracellular TGF α (APC) to intracellular TGF α (GFP) fluorescence by FACS and normalized this red:green ratio for all shRNAs to control shRNAs targeting lacZ. Most individual shRNAs showed no effect or had a normalized ratio with an absolute value less than ± 1 z-score from the distribution mean. Z-scores < 0 correspond to shRNAs with low red:green ratio, indicating enhanced TGF α shedding, and z-scores > 0 correspond to

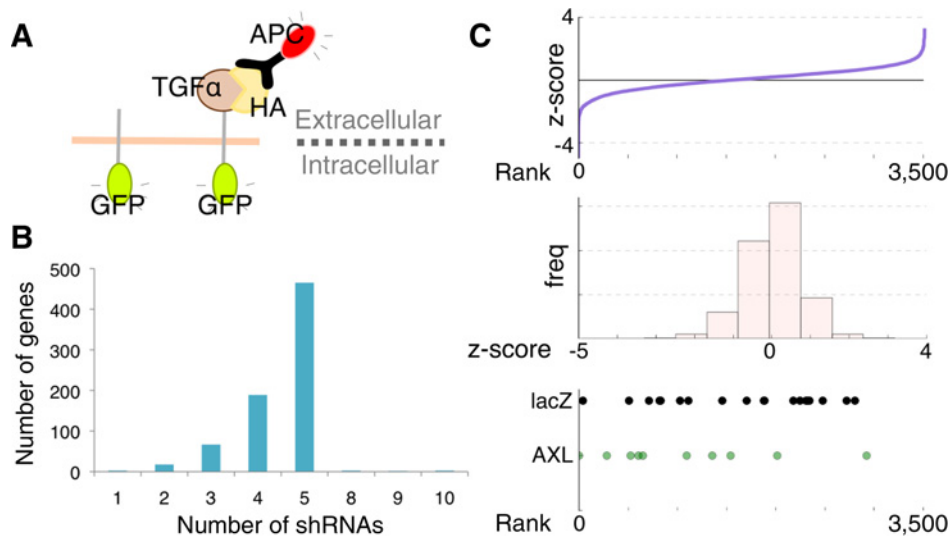


Figure 1.

An shRNA screen measured kinase and phosphatase effects on phorbol ester (TPA) induced TGF α shedding. **A**, Jurkat cells expressing HA-TGF α -GFP and lentiviral vectors either expressing shRNAs targeting the human kinome and phosphatome or lacZ-targeting control shRNAs were treated with TPA, stained with APC-coupled anti-HA antibody, and subjected to FACS. TGF α shedding was detected by determination of the mean red:green fluorescent ratio of the cells. **B**, shRNA coverage for most genes was 4–5 individual shRNAs/gene. **C**, Z-score normalized red:green ratios for all independent shRNAs relative to shlacZ controls plotted as a ranked distribution (top) and as a histogram of scores (middle). Z-scores < 0 correspond to shRNAs that had a low red:green ratio and enhanced TPA-induced shedding, and z-scores > 0 correspond to shRNAs which had a relatively high red:green ratio and prevented TPA-induced shedding. Bottom, all lacZ shRNAs (20 total) and all AXL shRNAs (10 total) fell within this distribution, and highlights the difficulty in determining which genes are consistently affecting shedding.

shRNAs with high red:green ratio and reduced TGF α shedding (ranked distribution in Fig. 1C, top and middle). A limited analysis validated the screen in principal by revealing that PKC α and the PKC-regulated protein-phosphatase-1-inhibitor-14D (PPP1R14D) are required for specific regulation of TGF α cleavage (4).

Within a given family of redundant shRNAs targeting the same gene, and also within samples targeted by the same control shRNA, resulting z-scores varied over a considerable range and overlapped significantly; shown as example for one targeted gene, *AXL*, and shLacZ controls (Fig. 1C, bottom). This demonstrates inherent difficulties similar to other shRNA screens in determining which shRNAs consistently produce a phenotype. We explored multiple ranking strategies before pursuing a computational network modeling approach to significantly improve upon these inherent problems.

A very stringent two-best shRNA scoring method used the average of multiple measurements for the same shRNA for z-score calculation and required a gene's top two shRNAs contain one hairpin that scored 2 z-scores and one hairpin that scored 1.5 z-scores above or below the mean; this method selected 5 genes. In contrast, a less stringent approach which calculated z-scores based on the median measurements of all redundant shRNAs targeting a given gene identified 22 genes with a z-score of 1 above/below the mean (in the positive/negative direction). The shEnrich method, explained in the next paragraph, selected the most targets of all the methods (Table 1). Each scoring method selected different and partially overlapping gene lists (comparison of the different scoring methods shown in Supplementary Table S1). *PRKCA* and *PPP1R14D* published in the original screen validation (4) scored in the 2 best shRNA and shEnrich methods, whereas other genes only scored in shEnrich.

Selection of gene candidates using the shEnrich method

To improve our scoring of genes identified in the original shRNA screen, we developed the shEnrich method to measure consistency of redundant shRNAs and strength of their effect. This enrichment scoring method is conceptually modeled after the original Gene set enrichment method (GSEA), and is representative of other rank-order methods for RNAi scoring (e.g., RIGER and dRIGER; refs. 50–53). These methods all developed ranking statistics that look for consistency of shRNA effects compared with the remainder of the tested shRNA population and control shRNAs.

Our method most closely resembles that of Kampmann and colleagues (53), in that our screening readout was a single measurement (z-score normalized red:green fluorescent ratios) and that we derived our null distributions from a cohort of nontargeting controls. However, that earlier approach does not correct for the number of shRNAs targeting a gene, which in our case ranged from 1 to 10. We therefore calculated expected distributions for each gene based on its shRNA family size; for example, for a gene with 4 shRNAs, we calculated 1,000 permutations using 4 shLacZs from our control set. Our enrichment method resulted in a projected z-score and a maximal normalized enrichment score (NES). This represents the rank at which maximal enrichment occurs for a gene's shRNA family. Fig. 2A represents the shEnrich score for *AXL* in the forward direction (highest rank reflects that an shRNA increased shedding) and for *PPP1R14D* in the reverse direction (highest rank indicates an shRNA decreased shedding). Both *AXL* and *PPP1R14D* show high

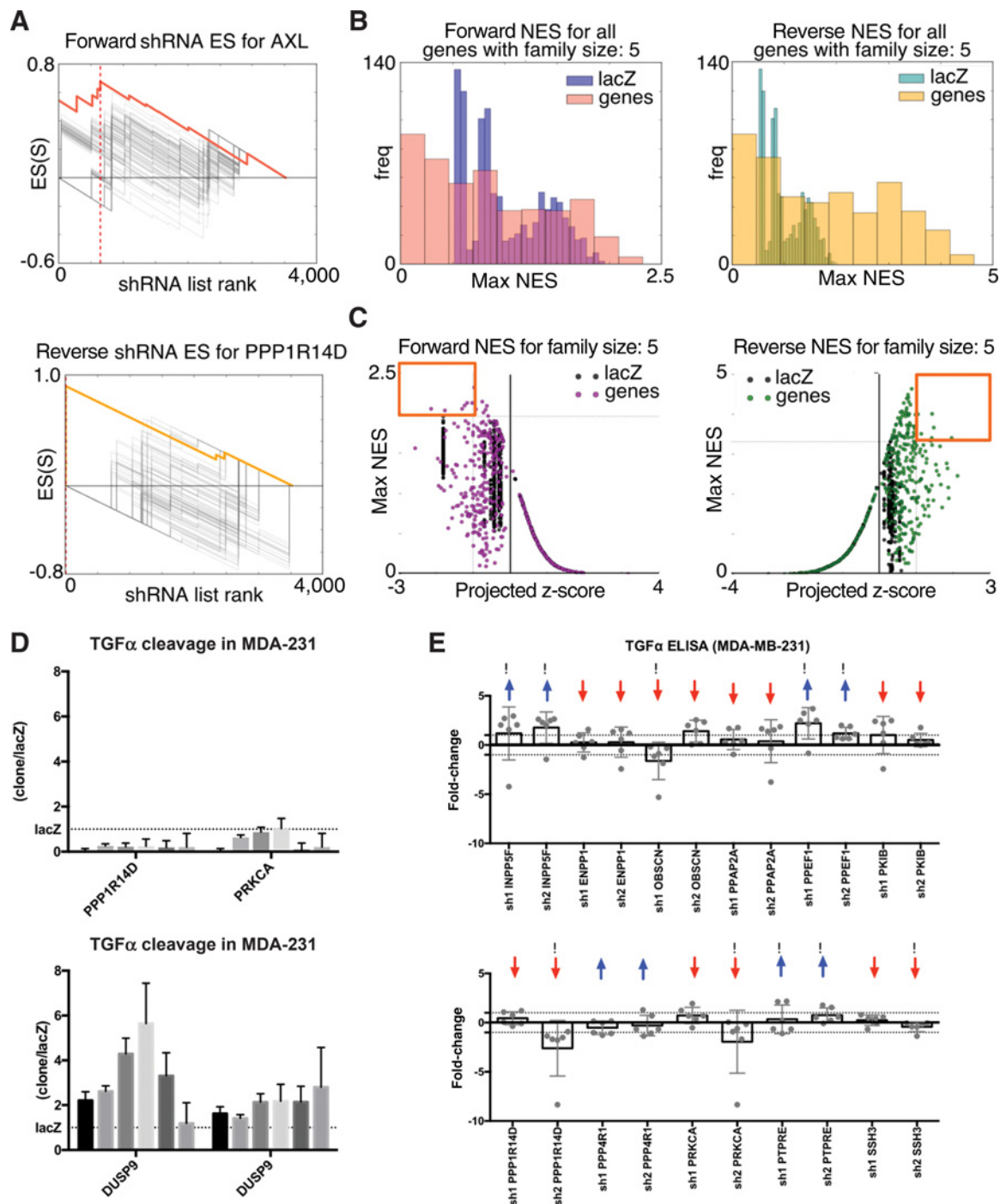
Table 1. Genes selected by the shEnrich method

shEnrich Method		
Forward shEnrich		
shRNA family size 2	<i>DDR2</i>	<i>PPP5C*</i>
<i>PPP2R1A</i>	<i>DKFZP566K0524</i>	<i>PRG-3</i>
<i>PTBP1*</i>	<i>DUSP13</i>	<i>PRKWNK3</i>
<i>RIOK2</i>	<i>EAT2</i>	<i>PTPRM*</i>
shRNA family size 3	<i>EEF2K*</i>	<i>RAF1*</i>
<i>CDC25A*</i>	<i>EIF2AK3</i>	<i>RIMS4</i>
<i>PTPN18</i>	<i>EPM2A</i>	<i>SGPP2</i>
<i>TP53RK</i>	<i>FBP2</i>	<i>SH2D1A*</i>
shRNA family size 4	<i>FLJ25449</i>	<i>SMG1*</i>
<i>BLK*</i>	<i>Gpr109b</i>	<i>SNRK*</i>
<i>CKM</i>	<i>GUCY2C</i>	<i>SPAP1</i>
<i>DUSP5*</i>	<i>IMPA2</i>	<i>SYT14L</i>
<i>EGLN1*</i>	<i>INPP5F</i>	<i>WWP2*</i>
<i>FLJ16518</i>	<i>IRAK1*</i>	shRNA family size 8
<i>GALK2</i>	<i>ITPKA</i>	<i>CIB2</i>
<i>GMFB</i>	<i>LOC283871</i>	<i>ERBB4*</i>
<i>HYPB</i>	<i>LOC401313</i>	
<i>INPP5B</i>	<i>LPPR4</i>	
<i>KIAA2002</i>	<i>MAP3K11*</i>	Reverse shEnrich
<i>LOC400687</i>	<i>MAP3K7IP1</i>	shRNA family size 2
<i>LOC441868</i>	<i>MAPK4</i>	<i>CALM1*</i>
<i>LOC90353</i>	<i>NRI3*</i>	<i>PPP2R1A*</i>
<i>LOC91461</i>	<i>NT5E</i>	<i>DUSP9</i>
<i>NEK7</i>	<i>NUDT11</i>	shRNA family size 3
<i>NUDT10</i>	<i>OBSCN*</i>	<i>PPAP2A</i>
<i>PHKA2*</i>	<i>PCTK3</i>	<i>SSH3</i>
<i>PINI*</i>	<i>PIB5PA</i>	shRNA family size 4
<i>PMVK</i>	<i>PIP5K1A</i>	<i>GPR109A</i>
<i>PTPN22*</i>	<i>PLCB4</i>	<i>LCK*</i>
<i>PTPN5</i>	<i>PPAPDC1</i>	<i>PPP1R14D</i>
<i>PTPRE</i>	<i>PPAPDC1A</i>	<i>SIK2*</i>
<i>RIPK5</i>	<i>PPEF1*</i>	<i>TRPV5*</i>
<i>RXR8</i>	<i>PPEF2*</i>	shRNA family size 5
<i>SACM1L</i>	<i>PPF1A1*</i>	<i>CDC14A*</i>
<i>TEX14</i>	<i>PPM1J</i>	<i>ENPP1</i>
<i>TRPM7*</i>	<i>PPP1R12B*</i>	<i>EPB41L4A</i>
shRNA family size 5	<i>PPP2CB*</i>	<i>NME5</i>
<i>ABL1*</i>	<i>PPP3CA*</i>	<i>PIM1*</i>
<i>AKAP11*</i>	<i>PPP4R1*</i>	<i>PKIB</i>
<i>CKS2*</i>	<i>PPP4R1L</i>	<i>PRKCA*</i>

NOTE: The shEnrich method selected genes that had consistent shRNA effects in the forward direction (shRNAs increased TPA-induced TGF α shedding) and in the reverse direction (shRNAs decreased TPA-induced TGF α shedding). Asterisks indicate genes that are included in following network analysis.

NES relative to the lacZ controls indicating high consistency. We repeated this process for all genes of all shRNA family sizes in both the forward (shRNAs increase shedding) and reverse (shRNAs decrease shedding) ranking directions. Within each family size (in forward and reverse direction), we compared gene shEnrich NES against 1,000 permutations calculated using subsets of the shLacZ controls. Figure 2B shows the distribution of shEnrich NES for all genes relative to the distribution of shLacZ scores for shRNA family size 5 (all other family sizes plotted in Supplementary Figs. S1 and S2). Most genes did not show an effect that was as consistent or more consistent than the shLacZ controls. To additionally filter gene candidates for strength of effect, we plotted gene shEnrich NES against the projected z-score (Fig. 2C). Many genes had a low shEnrich NES and a low projected z-score (low referring to a score with a value < -1 in the forward direction or $> +1$ in the reverse direction). Only a few genes had a high shEnrich NES and a relatively high projected z-score; these genes fell in the top left/top right quadrants (highlighted with orange squares) in the forward/reverse directions (scatter plots for all other family sizes shown in

Wilson et al.

**Figure 2.**

shEnrich selects genes for consistency and effect size. **A**, Lightning plots show the enrichment score for *AXL* in the forward direction (red, top) and *PPP1R14D* (gold, bottom) in the reverse direction. Gray lines represent 100/1,000 enrichment scores calculated for shlacZ. Dashed line represents position of maximal enrichment for the gene of interest. **B**, Normalized enrichment scores (NES) for all genes with 5 redundant shRNAs (family size 5) plotted against 1,000 NES for lacZ in the forward direction (left) and reverse direction (right). **C**, Maximal NES score for all genes with 5 redundant shRNAs and lacZ controls plotted against the z-score at which maximal enrichment occurs ('projected z-score'). Normalized distributions and maximal enrichment plots for all other gene family sizes are included in Supplementary Figures. **D**, Supernatant ELISA detection of cleaved TGF α in MDA-MB-231 cells with *PPP1R14D* and *PRKCA* knockdown (top), or *DUSP9* knockdown (bottom). Each bar represents redundant tests of the same shRNA; error bars are SEs of the ratio of shRNA gene:shlacZ control. Dotted line indicates measurements in respective shlacZ control. **E**, TGF α ELISA of additional genes identified by shEnrich method. Two shRNAs were selected for each gene and tested in sextuplicate in MDA-MB-231 cells. Bars represent average log₂ fold-change relative to a nontargeting control, and each dot represents an individual replicate. Red/blue arrows indicate the shEnrich prediction of directionality of effect (increased/decreased TGF α shedding) for each gene tested, and exclamation marks indicate where the experimental shRNA effect agreed with the shEnrich prediction.

Supplementary Fig. S3). For our example genes, *AXL* did not make the projected z-score cutoff of < -1 , but *PPP1R14D* did make the $> +1$ z-score cutoff. The full list of genes that passed these stringent criteria is shown in Table 1.

We first used a traditional strategy to validate a portion of shEnrich-identified gene targets in MDA-MB-231 cells, a triple-negative breast cancer cell line and well-studied cancer model, using an ELISA assay that detected cleaved TGF α ectodomain in cell culture supernatants. *PPP1R14D* or *PRKCA* knockdown blocked TGF α cleavage, again confirming our previously published results (4) and *DUSP9* knockdown increased shedding; results from six independent experiments are shown (Fig. 2D) using one shRNA for *PPP1R14D* and *PRKCA*, and (Fig. 2D, bottom) using two shRNAs for *DUSP9*. Knockdown of 11 other shEnrich-identified genes that induced strong effects on TGF α cleavage in the initial shRNA screen revealed that for 8 of the 11 gene targets, shRNAs showed consistent directionality of effect for both shRNAs tested in the MDA_MB-231 context (*INPP5F*, *ENPP1*, *PPAP2A*, *PPEF1*, *PKIB*, *PPP4R1*, and *PTPRE*), although effect size varied (Fig. 2E). Of the individual shRNAs, 10 of 22 had a directionality of effect consistent with the shEnrich prediction for their gene target (up or down arrows highlighted with exclamation points in Fig. 2E); the other shRNAs with shEnrich predictions showed opposite effects from the shEnrich predictions (arrows, but no exclamation points in Fig. 2E).

These effects may result from differences in effectiveness of knockdown depending on the cell type studied, as has been described in other reports (51) highlighting the importance of investigating a larger set of shRNAs per gene and using aggregate statistics such as shEnrich to analyze their effects. Detected switches in directionality suggest that contextual factors might affect the shedding phenotype, making it difficult to incorporate shRNA hits into signaling pathways from enrichment scores or targeted validation alone. We therefore performed additional analysis by network modeling to identify a more complete TGF α cleavage regulatory pathway.

PCSF identifies a TGF α shedding pathway

We previously described the role of off-target effects in RNAi or shRNA screens, specifically that both reagent-based and biology-based effects determine whether a gene can be identified as part of a pathway based on gene knockdown data (43). Interpreting RNAi or shRNA results in a network framework, in contrast to an individual "hits" or "targets" framework, leverages contributions from all hit/target contributions to pathways via their relationships with other network genes. This interpretation can ameliorate dependence upon individual reagent performance and increase confidence in biological validation.

Our previous work demonstrated that data integration into a network context could construct novel pathways despite noise from RNAi screens (54). Starting with results obtained from shEnrich, we used the PCSF method (46, 55) to construct a pathway for TGF α cleavage; the method predicted additional pathway genes not identified in the initial experimental set in this process. The PCSF acted as a filter, and required genes to have interaction associations with other genes identified from the screen to be included in the final pathway. To define all sets of possible associations, we derived an interactome from iRefWeb and added predicted kinase and phosphatase site-specific interactions from Networkin and DEPOD (refs. 45, 56; details of the interactome construction are explained in Materials and Methods;

optimization of network node selection is shown in Supplementary Fig. S4). The algorithm identified an optimal subnetwork from this interactome by selecting edges that captured genes from the shEnrich method ("experimental genes") without overfitting. In this process, the algorithm added predicted genes that connected experimental genes (Fig. 3, top). We used a set of parameters to tune the algorithm to ensure an appropriate selection of experimental and predicted genes (see Materials and Methods). This optimized network contained 86 genes, and 97 edges. Of the original 108 genes selected from the shEnrich method, 43 were retained. Of note, the network contained interaction evidence for the experimental genes *PPEF1*, *OBSCN*, *DUSP9*, *PRKCA*, and *PPP4R1*; these genes were selected by shEnrich and confirmed with ELISA in MDA-MB-231 cells. *PPP1R14D* was not included despite experimental validation, suggesting that there is not sufficient interaction evidence to include this gene in the pathway. The remaining 43 genes were previously unidentified genes predicted by the algorithm to be relevant to TGF α cleavage. These predicted genes also included gene targets contained in the original screen that were refractory to knockdown using available shRNAs.

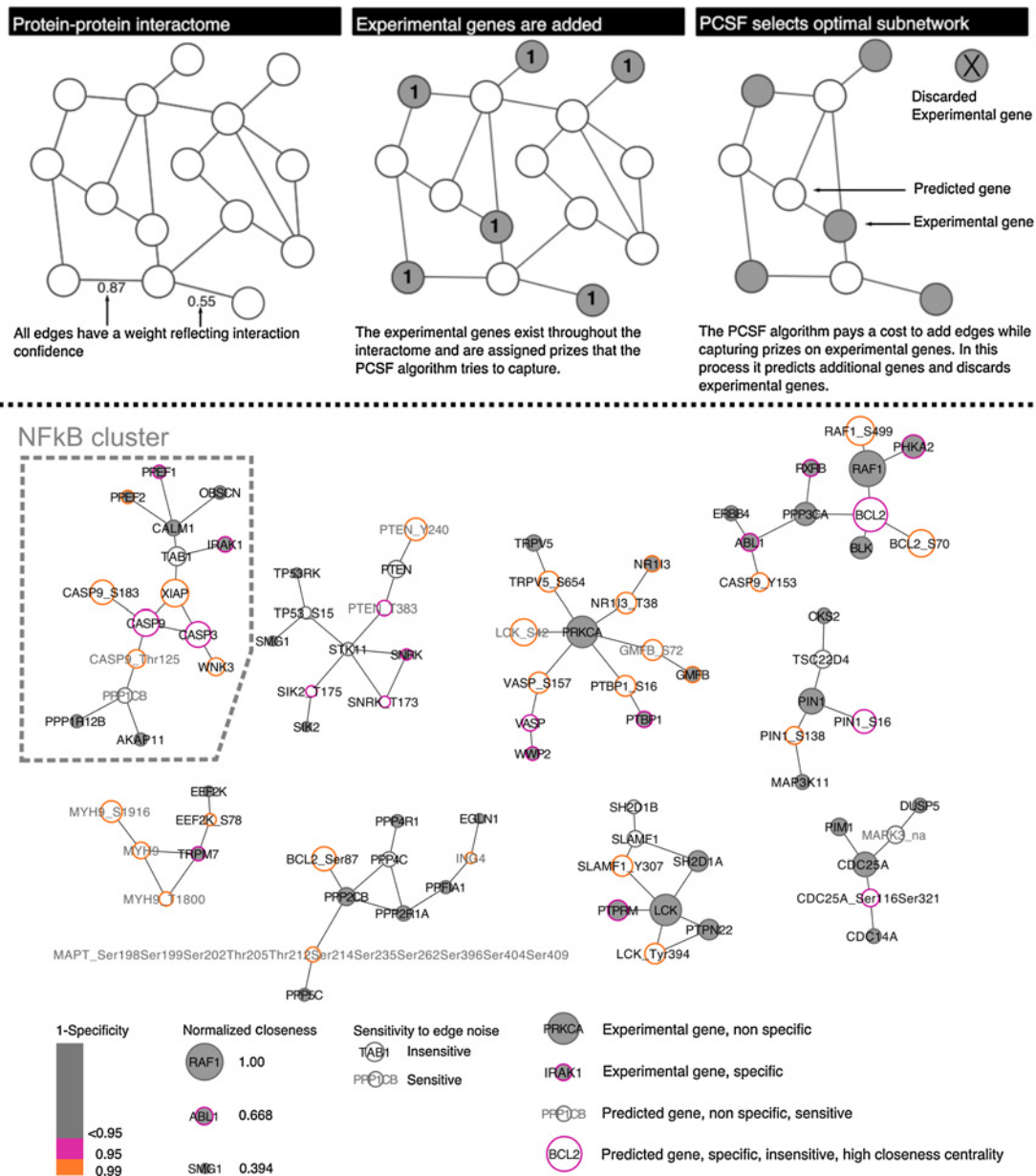
We hypothesized that the optimized network gene list contained subsets of functionally related genes. To find these subsets, we leveraged edges in the network solution. Genes with a high number of interneighbor edges are more likely to have functional similarities. We used the GLay Community clustering Cytoscape plug-in (57) to subdivide the optimized network into a final target set of 9 network submodules. This process removed 14 edges and retained all genes (Fig. 3, bottom; full network shown in Supplementary Fig. S5).

Robustness analysis prioritizes predicted pathway genes

To prioritize candidates selected by PCSF, we performed a series of robustness and connectivity analyses. Here we explain the metrics for gene prioritization and the corresponding quantification as presented in Table 2. We measured the sensitivity of each gene in the solution by counting representation in 100 runs of PCSF with noise added to the edges. Genes that are insensitive to noise show up in all networks and are assigned a score of 0.00, whereas genes that are sensitive appear in a few networks only and are assigned a score equal to 1-fraction of networks in which they are represented. A score of 0.99 indicates that the gene was present in only one network. None of the experimental genes identified by shEnrich were sensitive to edge noise (high aggregate score; Table 2, left column); however, 12 of the newly predicted genes were highly sensitive and showed up only in the solution without edge noise (Table 2, genes with low aggregate score bottom of right column). This suggests that low probability edges connected these predicted genes to the network; varying the edge value caused the algorithm to remove the predicted gene in some simulations.

We then tested specificity of the network solution using random inputs from the targets in the original shRNA library. This process involved selecting random sets of genes from the original library (regardless of whether they scored using our shEnrich method), rerunning the PCSF routine at the optimal parameters and counting gene representation in this family of 100 random networks. Gene border color indicates fractional representation in these 100 random networks (Fig. 3, bottom). Of the 43 experimental genes, 30 genes showed low specificity, indicating general association among targets from the original library. These targets may still have a role in shedding regulation (such as *PRKCA*); however, we

Wilson et al.

**Figure 3.**

PCSF identifies TGF α shedding regulatory network. Top, the cartoon schematic represents how PCSF selects an optimal subnetwork. Interaction edges are aggregated from multiple databases and all edges are scored (two shown for simplicity). Prizes are assigned from experimental data; in our case prizes were assigned to genes selected by shEnrich. The algorithm weights the cost of adding edges with capturing prizes in selecting an optimal network. Bottom, the optimal, clustered network contains 86 genes and 83 edges. Gray face coloring indicates genes selected from the original experimental data set; white face represents predicted gene (genes and phospho-sites) selected by the algorithm. Gene border represents specificity to randomization (pink, <0.1 ; orange, <0.05), and gene size represents closeness centrality (larger genes are more central and more robust). Gray gene labels indicate genes that are sensitive to edge noise. Genes on the far right of the legend below the networks are annotated examples to help interpret all of their network properties. The cluster associated with Nf κ B signaling is highlighted.

could not distinguish these effects from general library association.

We further used centrality metrics to quantify the robustness of our network selections. Centrality did not imply a biological centrality per se, but reflected how the genes were selected in this network solution. Having a high centrality implied a greater resilience to experimental noise from the input set; mathemati-

cally, centrality reflects how interaction edges contributed to a gene's presence in the final network. We calculated the degree, betweenness, page-rank, and closeness centrality, and an aggregate score (Supplementary Fig. S6A) based on interactions in the original, unclustered network. We created a normalized histogram of centrality scores to evaluate the relative distribution of values (Supplementary Fig. S6B). From this histogram, we

Table 2. Experimental and predicted genes ranked by multiple robustness metrics

Experimental genes	Sensitivity	1-Specificity	Normalized closeness	Aggregate score	Predicted genes	Sensitivity	1-Specificity	Normalized closeness	Aggregate score
LCK	0.00	0.891	0.920	0.963	BCL2	0.00	0.901	0.964	0.975
RAF1	0.00	0.723	1.000	0.956	RAF1_S499	0.00	0.950	0.876	0.961
PHKA2	0.00	0.941	0.780	0.936	BCL2_S70	0.00	0.970	0.849	0.958
PIN1	0.00	0.871	0.821	0.935	XIAP	0.00	0.950	0.851	0.955
PRKCA	0.00	0.713	0.923	0.935	CASP9	0.00	0.941	0.835	0.950
PTPRM	0.00	0.921	0.730	0.921	CASP3	0.00	0.931	0.821	0.945
PPP3CA	0.00	0.851	0.774	0.920	CASP9_S183	0.00	0.960	0.799	0.944
BLK	0.00	0.861	0.758	0.918	BCL2_Ser87	0.00	0.950	0.795	0.941
SH2D1A	0.00	0.851	0.738	0.911	PIN1_S16	0.00	0.941	0.786	0.938
PTPN22	0.00	0.832	0.732	0.907	SLAMF1_Y307	0.00	0.990	0.738	0.933
ABL1	0.00	0.901	0.668	0.902	NR1I3_T38	0.00	0.990	0.736	0.933
NR1I3	0.00	0.960	0.609	0.897	PTBP1_S16	0.00	0.970	0.736	0.930
RXR8	0.00	0.911	0.635	0.895	LCK_Tyr394	0.00	0.970	0.732	0.929
GMFB	0.00	0.950	0.609	0.895	VASP_S157	0.00	0.950	0.739	0.928
PIM1	0.00	0.881	0.654	0.895	TRPV5_S654	0.00	0.950	0.736	0.927
PPP2CB	0.00	0.842	0.673	0.894	CASP9_Y153	0.00	0.990	0.688	0.921
PTBP1	0.00	0.901	0.609	0.887	PIN1_S138	0.00	0.950	0.670	0.910
TRPV5	0.00	0.891	0.609	0.886	WNK3	0.00	0.950	0.667	0.909
IRAK1	0.00	0.911	0.587	0.883	CDC25A_Ser116Ser321	0.00	0.931	0.656	0.904
CKS2	0.00	0.881	0.563	0.873	TAB1	0.00	0.842	0.703	0.901
CDC14A	0.00	0.891	0.554	0.872	TSC22D4	0.00	0.871	0.670	0.898
DUSP5	0.00	0.891	0.554	0.872	VASP	0.00	0.941	0.614	0.895
TRPM7	0.00	0.911	0.540	0.872	SLAMF1	0.00	0.891	0.616	0.887
CDC25A	0.00	0.505	0.801	0.872	PPP4C	0.00	0.881	0.572	0.875
MAP3K11	0.00	0.871	0.563	0.871	SH2D1B	0.00	0.891	0.525	0.865
WWP2	0.00	0.931	0.524	0.871	PTEN	0.00	0.683	0.656	0.864
PPEF2	0.00	0.950	0.509	0.870	EEF2K_S78	0.00	0.950	0.470	0.861
PPEF1	0.00	0.941	0.509	0.869	SIK2_T175	0.00	0.921	0.442	0.849
PPP2R1A	0.00	0.822	0.574	0.866	SNRK_T173	0.00	0.911	0.441	0.847
ERBB4	0.00	0.802	0.562	0.860	TP53_S15	0.00	0.644	0.443	0.805
OBSCN	0.00	0.881	0.509	0.859	STK11	0.00	0.535	0.503	0.803
AKAP11	0.00	0.891	0.497	0.858	LCK_S42	0.99	0.990	0.842	0.373
CALM1	0.00	0.733	0.594	0.857	PTEN_Y240	0.99	0.970	0.768	0.351
PPP5C	0.00	0.891	0.489	0.856	MYH9_S1916	0.99	0.980	0.751	0.348
PPP4R1	0.00	0.881	0.493	0.855	GMFB_S72	0.99	0.980	0.736	0.345
PPP1R12B	0.00	0.871	0.497	0.855	CASP9_Thr125	0.99	0.960	0.685	0.329
SNRK	0.00	0.911	0.441	0.847	MYH9	0.99	0.980	0.630	0.318
PPFIA1	0.00	0.802	0.497	0.844	MAPT_Ser198Ser199Ser202Thr205Thr212Ser214Ser235Ser262Ser396Ser404Ser409	0.99	0.950	0.568	0.298
EEF2K	0.00	0.851	0.415	0.831	MYH9_T1800	0.99	0.990	0.538	0.297
SIK2	0.00	0.871	0.393	0.829	PTEN_T383	0.99	0.921	0.571	0.294
EGLN1	0.00	0.851	0.390	0.825	MAPK3_na	0.99	0.782	0.656	0.293
TP53RK	0.00	0.822	0.394	0.821	ING4	0.99	0.960	0.438	0.268
SMG1	0.00	0.802	0.394	0.818	PPP1CB	0.99	0.723	0.579	0.265

NOTE: Experimental genes (left) and predicted genes (right) were ranked by the following metrics: sensitivity represents fractional representation in a family of 100 networks created with 0.5% noise added to the interactome edges; specificity represents the fractional representation in a family of 100 networks created with random inputs and 1-specificity is used for ranking as low specificity indicates robustness to this type of randomization; normalized closeness centrality reflects a node's robustness as this metric indicates association to other nodes within the network; aggregate score was calculated by weighting each metric by the SD for that metric and normalizing to the maximum score possible for all experimental/predicted genes.

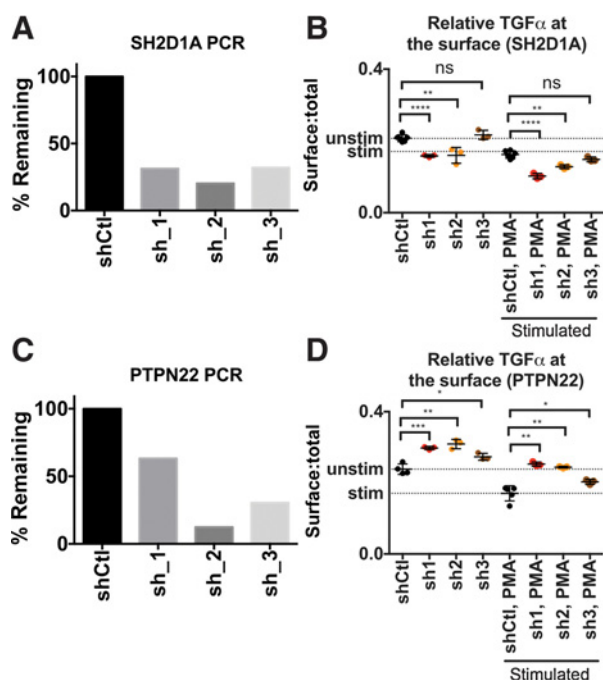
observed that closeness centrality best discerns connectivity, while other metrics are dominated by a few high-value nodes (i.e., page-rank, betweenness, and degree centrality). Using closeness centrality, we visualized these genes within the network solution by adjusting their symbol size to reflect extent of connectivity (Fig. 3; quantification in Table 2). Finally, we created a normalized, aggregate score (Table 2) reflecting an experimental gene's performance across these three metrics. We adjusted specificity/sensitivity to be $(1 - \text{specificity}) / (1 - \text{sensitivity})$, and normalized closeness centrality to the max value to scale all metrics from 0 to 1. We weighted each metric by the SD for that metric and normalized to the maximum score possible for all experimental genes (Table 2, left). We completed a similar analysis for predicted

genes in the network, and again measured sensitivity to edge noise, specificity using random input terminals, and closeness centrality as a metric for connectivity (Table 2, right).

Experimental validation of PCSF-selected network genes

First, we validated PCSF-selected experimental gene hits from the original screen. SLAM-associated protein (SAP; *SH2D1A*) and Protein Tyrosine Phosphatase, Non-Receptor Type 22 (*PTPN22*), using our FACS-based TGF α shedding assay in Jurkat cells with or without TPA stimulation. We used TPA stimulation as a benchmark to explore whether our gene perturbations were of similar magnitude to a known modulator of TGF α shedding. Knockdown of *SH2D1A* was monitored by qPCR, demonstrating

Wilson et al.

**Figure 4.**

Validation of effect of experimental genes on TGF α cleavage in Jurkat cells. **A**, Knockdown of *SH2D1A* was monitored by qPCR. **B**, Knockdown of *SH2D1A* with three individual shRNAs enhanced TPA-stimulated TGF α cleavage from the cell surface compared with control shRNA-expressing cells (indicated by lower red:green fluorescent ratio as compared with control). **C**, Knockdown of *PTPN22* was monitored by qPCR. **D**, Knockdown of *PTPN22* with three individual shRNAs decreased TPA-stimulated TGF α cleavage as compared with control shRNA (indicated by higher red:green fluorescent ratio as compared with control). Error bars, SEM. We used an unpaired *t* test to test significance. *, $P \leq 0.05$; **, $P \leq 0.01$; ***, $P \leq 0.001$; ****, $P < 0.0001$.

70%–80% decrease of *SH2D1A* mRNA levels for all three individual shRNAs (Fig. 4A). Knockdown of *SH2D1A* with three individual shRNAs enhanced TPA-stimulated TGF α cleavage from the cell surface as determined by decreased red:green fluorescent ratio compared with TPA-stimulated control shRNA-expressing cells (Fig. 4B). Again, mRNA knockdown for each individual shRNA against *PTPN22* was monitored by qPCR and varied between 40% and 90% (Fig. 4C). In contrast to *SH2D1A*, three shRNAs targeting *PTPN22* decreased TPA-stimulated TGF α cleavage (increased red:green ratio) as compared with control shRNA (Fig. 4D); Three other genes contained in the original screen (*OBSCN*, *PPEF1*, and *PRKCA*) and present in our network model were already validated in MDA-MB-231 triple-negative breast cancer cells by ELISA measurements in the context of our shEnrich method validation (Fig. 2E). Knockdown of *SH2D1A* or *PTPN22* in MDA-MB-231 cells confirmed their effects on TPA-induced TGF α cleavage in this cell type (enhanced cleavage after *SH2D1A* and reduced cleavage after *PTPN22* knockdown), as measured by ELISA (Supplementary Fig. S7A, knockdown efficiency shown in Supplementary Fig. S7B).

We next validated PCSF-selected predicted genes not found in the original screen. Our optimized network contained a 15-gene cluster with high centrality, specificity, and low sensitivity (Fig. 3). Of these genes, 7 were from the original screen: *PPEF1*, *PPEF2*,

OBSCN, *CALM1*, *IRAK1*, *PPP1R12B*, and *AKAP11*. By shEnrich analysis, 6 of these genes decreased TGF α shedding, except for *AKAP11* that induced shedding (lightening plots in Supplementary Fig. S8B–S8H). We then tested the effect of knockdown of two predicted genes contained in this cluster, X-linked-inhibitor-of-apoptosis (*XIAP*) and TGF-Beta-Activated-Kinase-1-Binding-Protein-1 (*TAB1*) for their effect on TGF α shedding. We selected these predicted genes because they were robust among this cluster (Table 2, right column). As we constructed this pathway using a tissue nonspecific interactome, we also explored the expression of this regulatory cluster in Jurkat, MDA-MB-231, Kato-III, and MKN-45 cell lines (Supplementary Fig. S8I) using CCLE data and found that all components were expressed (47). We monitored mRNA knockdown by qPCR in the presence of three shRNAs against *TAB1* (Fig. 5A). *TAB1* knockdown decreased TPA-stimulated TGF α cleavage from the cell surface (increased red:green fluorescent ratio) as compared with TPA-stimulated control shRNA-expressing cells (Fig. 5B). *XIAP* mRNA knockdown (Fig. 5C) decreased surface-bound TGF α (decreased red fluorescence) as compared with control shRNA (Fig. 5D). Additional experiments evaluating the effect of *TAB1* or *XIAP* knockdown on TGF α shedding in Jurkat cells are shown in Supplementary Fig. S9A–S9D. We also confirmed the same effects of *TAB1* and *XIAP* knockdown on TGF α cleavage in MDA-MB-231 triple-negative breast cancer cells (Supplementary Fig. S9E) and monitored mRNA expression after shRNA perturbation (Supplementary Fig. S9F). Taken together, these results confirmed the relevance of PCSF-identified experimental and predicted network genes in TGF α cleavage regulation.

Network modeling identifies intersection between genes that regulate inflammation and ectodomain cleavage

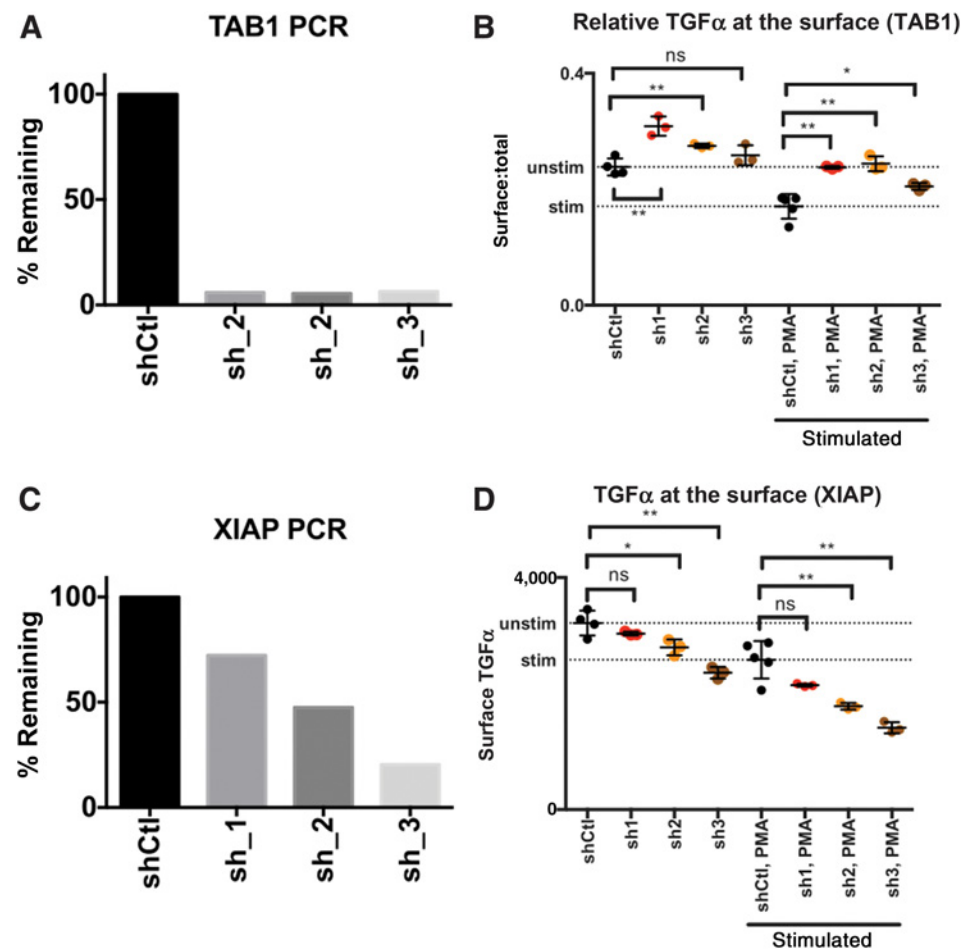
As it is widely accepted that inflammation contributes significantly to cancer pathogenesis (reviewed in ref. 58), it is interesting to note that most genes contained in our PCSF-identified 15-gene TGF α -regulatory cluster are associated with the NF κ B pathway, suggesting a mechanistic link between the release of tumor growth factors such as TGF α and inflammation. Here we hypothesized that our gene cluster was relevant for understanding cancer pathology and that testing of an existing chemical inhibitor against the predicted gene, *IRAK1*, could lend mechanistic understanding of how this inhibitor could be applied clinically.

To explore the relevance of genes contained in our 15-gene "TGF α /NF κ B regulatory cluster" and growth factor release in cancer, we first examined their normalized expression in various cancers by analyzing cBioPortal data (59) and differential expression in human cancer cell lines from Expression Atlas (48). We focused on the upper subset of already validated "TGF α /NF κ B regulatory cluster" genes, *PPEF1*, *PPEF2*, *OBSCN*, *CALM1*, *XIAP*, *TAB1*. We observed that the genes in this subset are expressed in multiple cancer types, including in gastric cancer, but none of them at significantly different levels when compared between cancers (Fig. 6A–E). However, some subsets of components were differentially expressed in multiple cancer types (log₂ fold-change in Fig. 6F; *P* values in Supplementary Fig. S10, and data accession numbers in Supplementary Table S2). *IRAK1* is most overexpressed in glioblastoma multiforme, astrocytoma, hepatocellular carcinoma, and liver cancer from cell line data (Fig. 6F).

Although we validated the effect of some of these NF κ B-regulatory genes on TGF α cleavage (Fig. 5; Supplementary Fig. S9), two inhibitors of *IRAK1* had no effect on TGF α cleavage.

Figure 5.

Validation of predicted genes on TGF α cleavage in Jurkat cells. **A**, Knockdown of *TAB1* was monitored by qPCR. **B**, Knockdown of *TAB1* with three individual shRNAs decreased TPA-stimulated TGF α cleavage from the cell surface as compared with control shRNA-expressing cells (indicated by higher red:green fluorescent ratio as compared with control). **C**, Knockdown of *XIAP* was monitored by qPCR. **D**, Knockdown of *XIAP* with three individual shRNAs decreased TGF α at the cell surface as compared with control shRNA (indicated by lower red fluorescence as compared with control). Error bars, SEM. We used an unpaired *t* test to test significance. *, $P \leq 0.05$; **, $P \leq 0.01$; ***, $P \leq 0.001$; ****, $P < 0.0001$.



Furthermore, an inhibitor of IKK β [upstream of NF κ B; controls the phosphorylation and subsequent degradation of one important direct regulator of NF κ B (I κ B)] did not affect TGF α cleavage (Fig. 6G and H). This suggests that the NF κ B-regulatory function of this gene cluster is not required for their effect on TGF α cleavage. In addition, these results suggest that IRAK1 inhibitors do not modulate TGF α cleavage.

In summary, these results suggest that tumor-associated inflammation may enhance tumor growth by also enhancing growth factor release due to overlap in their regulatory pathways and suggests unexpected novel applications for inhibition of NF κ B-regulatory genes in combination targeted therapies in cancer.

Discussion

Here we report a putative TGF α shedding pathway through a combined computational and experimental approach and demonstrated the relevance of this pathway for targeted therapy design. We identified a cohort of genes organized in subnetworks that affect TGF α ectodomain release, vetted these selections computationally, and validated genes using targeted experiments in several cancer cell types. In the process, we identified an unexpected connection between regulators of the NF κ B pathway and the release of cancer growth factors of the EGFR ligand family by ectodomain cleavage.

While the identified genes tune TGF α shedding and thus EGFR activation, many of them are not predicted oncogenes by traditional expression, mutation, or activation metrics. Our approach thus further highlights a trend toward selecting therapeutic targets based on functional role rather than overexpression of a particular gene in diseased over normal tissue. It is important to note that our network modeling approach yielded predicted genes not previously tested in our shRNA screen and that we could not have predicted these genes using traditional metrics. The directionality of their effect on TGF α regulation cannot be predicted, and discovering directionality requires dedicated experimental validation (see also discussion of the predicted gene *XIAP* below). Furthermore, we made these predictions in a tissue, nonspecific manner, but were able to validate these genes in multiple cell lines. The results show that we can discover alternative control mechanisms for growth factor pathway activation regardless of tissue type and that these targets require novel methods for discovery.

We explored the relevance of this pathway for cancer therapeutics and specifically investigated whether there was a link between the NF κ B pathway and TGF α shedding. The literature supports the role of these genes in regulating NF κ B signaling and there are several observations that suggest that more indirect connections and coregulation of the EGFR and NF κ B pathways indeed exist. In head and neck squamous cell carcinoma, *EGFR* and *TGFA* genes are upregulated concurrently with NF κ B signaling components.

Wilson et al.

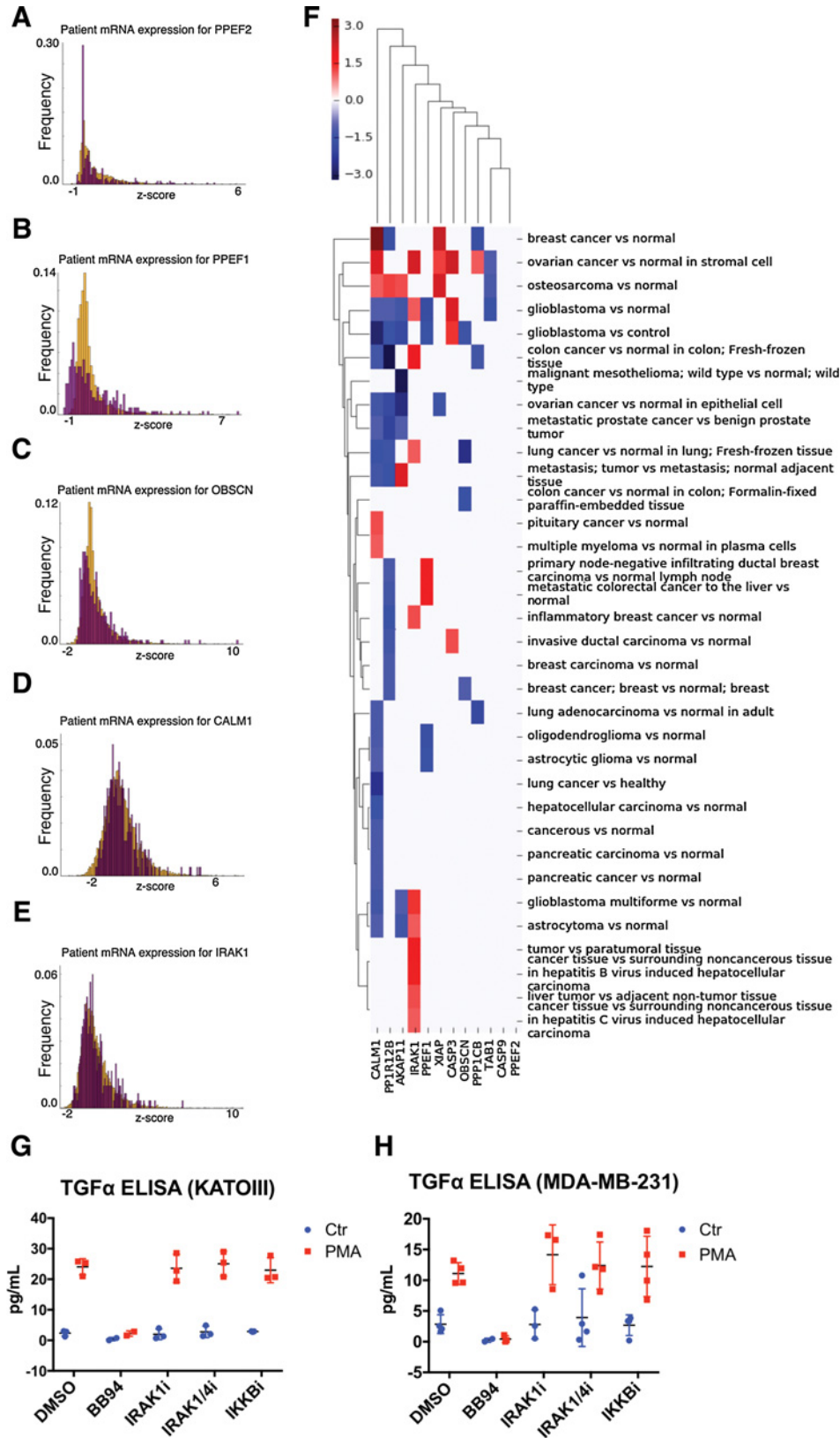


Figure 6. Analysis of genes in the "TGF α /NF κ B regulatory cluster". **A-E**, mRNA expression of network genes in human cancer samples. Histograms represent distribution of mRNA z-scores for PPEF2 (**A**), PPEF1 (**B**), OBSCN (**C**), CALM1 (**D**), and IRAK1 in gastric cancer (orange; 302 samples) and "other" cancers (purple; 10,550 samples; also see Materials and Methods; **E**). **F**, Differential expression of genes of the TGF α /NF κ B regulatory cluster in multiple cancer types from Expression Atlas. Colorbar indicates log₂ fold-change as reported from Expression Atlas. Kato-III (**G**) or MDA-MB-231 (**H**) cells were treated with vehicle (DMSO), the metalloprotease inhibitor BB94, IRAK4 inhibitor, IRAK1/4 inhibitor, or IKK inhibitor for 1 hour and exposed to control treatment or TPA (100 nmol/L) for 30 minutes. TGF α release was measured in cell supernatants by ELISA. Error bars, SEM.

The NF κ B activators, IKK α and IKK β enhance EGFR signaling, and activation of both IKKs can induce EGFR, TGF α , and Jun expression, a downstream effector of EGFR (60). Gastric *H. pylori* infection induces activation of EGFR and NF κ B activity and both are thought to be associated with gastric cancer progression (61, 62). NF κ B has been associated with resistance to EGFR therapies in cancer and inhibition of NF κ B is able to sensitize cells to erlotinib treatment. Anti-EGFR therapies were indeed able to reduce NF κ B activation (reviewed in ref. 10). Furthermore, it is well established that stimulation of EGFR can activate NF κ B through proteasome-mediated degradation of I κ B α (63, 64). Patient and cell line expression data validated our first hypothesis that these network components are expressed in cancer samples, albeit at varying levels in different cancers, and possibly relevant to pathology. Our experimental validation confirmed the network-based hypothesis that *TAB1* and *XIAP* affect TGF α shedding. Our experiments with chemical inhibitors of IRAK1 or of I κ B suggest that the NF κ B-regulatory function of these genes is not needed for their cleavage regulatory function, and thus, we were unable to confirm a mechanistic hypothesis about inhibitor mode of action. We sought to validate the role of IRAK1 in tuning TGF α shedding in gastric cancer because these cancers are growth factor-driven and exhibit EGFR pathway dependencies. However, from our cancer cell line analysis, it appears that our NF κ B-related cluster is differentially expressed in brain and liver cancers, which are not traditionally EGFR pathway driven. Further analysis may explore the role of IRAK1 inhibitors in these cancers as opposed to gastric cancers.

Our network model predicts new mechanistic information about *XIAP*, a gene that is currently a focus for therapeutic development. *XIAP*-*TAB1* binding is an upstream regulator of NF κ B signaling (65) and overexpression of *XIAP* is associated with loss of apoptotic signaling in cancer (66). *XIAP* binds and inhibits caspases 3 and 9, and also TAK1; binding TAK1 causes ubiquitination and degradation of TAK1 to prevent its activation of JNK (67). NF023, a new compound, inhibits *XIAP*-*TAB1* binding, and thus could act as a proapoptotic therapeutic in cancer (65). Our work complements these efforts by predicting an additional functional role for *XIAP*: *XIAP* targeting can also affect EGFR signaling by modulating TGF α cleavage. This information could indicate when *XIAP* intervention might be clinically useful. Although *XIAP*-*TAB1* interaction is necessary for activation of NF κ B signaling, knockdown of *XIAP* and *TAB1* proteins individually have opposite effects on TGF α cleavage. This suggests that their cleavage regulatory function is independent of their functions in NF κ B signaling. Experimental validation determined the directionality of predicted genes' effect on TGF α shedding because our model did not describe this directionality.

Our focus here has been on signaling pathway nodes, as a category generally offering potential for therapeutic targeting. This focus differs from an earlier study in which the Kveiborg laboratory undertook a genome-wide screen for regulators of HB-EGF shedding (like TGF α also an EGFR ligand ADAM17 substrate; ref. 68). On the basis of selection criteria requiring that at least three of four individual siRNAs inhibited HB-EGF shedding after TPA treatment, they validated 81 genes, including ADAM17 and PKC α . The signaling nodes obtained in their study corresponded well with the findings in our screen. Further stringent retesting of these initial hits confirmed that 24 hits mimicked the effects of ADAM17 knockdown on HB-EGF cleavage, including the multifunctional sorting protein PACS2 as a top hit. PACS2 was shown

to colocalize with ADAM17 on early endosomes and to regulate recycling and stability of internalized ADAM17, thereby sustaining ADAM17 cell-surface activity by diverting ADAM17 away from degradation. The fact that the main finding of this screen represents an ADAM17 trafficking factor might be related to the significantly longer time frame of induced shedding stimulation in the screen (30 minutes vs. 2–5 minutes in our screen). Shedding can occur within seconds to minutes, while trafficking usually requires more time. This suggests that the genes we identified might act on regulatory components that do not require trafficking (or transcription). Similar to our screen results, hits were segregated into multiple functional categories but no enrichment in particular signaling pathways was found. This further emphasized the need for novel network modeling approaches as we performed and validated them in the current work. Future work will have to address whether the regulators we identified act on the protease, the substrate (TGF α) or other proteins that interact with ADAM, substrate or both (12), and by what mechanism they affect cleavage. In this context, particularly if they act on the protease, we need to explore the possibility that our regulators also affect the cleavage of other ADAM substrates beyond TGF α .

In summary, our work identified and validated numerous regulatory components of TGF α shedding that could be leveraged for multiple treatment and disease contexts. These genes may be relevant as novel therapeutic targets in contexts where EGFR signaling is hyperactive or where EGFR is a source of therapeutic resistance. While we focus primarily on cancer, this pathway model is relevant for other diseases that are strongly affected by EGFR signaling, such as organ fibrosis or inflammation (8). Our network modeling approach proves useful for identifying how signaling pathways intersect or overlap and can thus affect targeted therapies. Our pathway analysis lays the ground-work for identifying signaling intermediates that bridge multiple pathways to affect the release of growth factors in the tumor environment. While discovering how these pathways intersect remains a difficult challenge, our analysis demonstrates a path toward target selection and considering mechanistic implications of therapeutic interventions.

Disclosure of Potential Conflicts of Interest

No potential conflicts of interest were disclosed.

Authors' Contributions

Conception and design: J.L. Wilson, E. Kefaloyianni, E. Fraenkel, D.A. Lauffenburger, A. Herrlich

Development of methodology: J.L. Wilson, L. Stopfer, E. Fraenkel

Acquisition of data (provided animals, acquired and managed patients, provided facilities, etc.): J.L. Wilson, E. Kefaloyianni, L. Stopfer, C. Harrison, V.S. Sabbisetti

Analysis and interpretation of data (e.g., statistical analysis, biostatistics, computational analysis): J.L. Wilson, E. Kefaloyianni, L. Stopfer, C. Harrison, V.S. Sabbisetti, E. Fraenkel, A. Herrlich

Writing, review, and/or revision of the manuscript: J.L. Wilson, E. Kefaloyianni, L. Stopfer, V.S. Sabbisetti, D.A. Lauffenburger, A. Herrlich

Administrative, technical, or material support (i.e., reporting or organizing data, constructing databases): V.S. Sabbisetti, A. Herrlich

Study supervision: E. Fraenkel, D.A. Lauffenburger, A. Herrlich

Acknowledgments

This work was partially supported by NIH grant U01-CA155758 (to D.A. Lauffenburger), NIH grant R01-CA096504 (to D.A. Lauffenburger), U01-CA184898 (to E. Fraenkel), NIDDKR00DK077731 and NIDDKR01DK108947 (to A. Herrlich). Computing resources were partially supported by the National Science Foundation grant DBI-0821391.

Wilson et al.

The authors would like to thank Brian Joughin for helpful discussions in designing and troubleshooting the shEnrich method.

The costs of publication of this article were defrayed in part by the payment of page charges. This article must therefore be hereby marked

advertisement in accordance with 18 U.S.C. Section 1734 solely to indicate this fact.

Received March 19, 2017; revised August 16, 2017; accepted October 4, 2017; published OnlineFirst October 10, 2017.

References

- Chen J, Zeng F, Forrester SJ, Eguchi S. Expression and function of the epidermal growth factor receptor in physiology and disease. *Physiol Rev* 2016;96:1025–69.
- Borrell-Pagès M, Rojo F, Albanell J, Baselga J, Arribas J. TACE is required for the activation of the EGFR by TGF- α in tumors. *EMBO J* 2003;22:1114–24.
- Horiuchi K, Le Gall S, Schulte M, Yamaguchi T, Reiss K, Murphy G, et al. Substrate selectivity of epidermal growth factor-receptor ligand sheddases and their regulation by phorbol esters and calcium influx. *Mol Biol Cell* 2007;18:176–88.
- Dang M, Armbruster N, Miller MA, Cermenio E, Hartmann M, Bell GW, et al. Regulated ADAM17-dependent EGF family ligand release by substrate-selecting signaling pathways. *Proc Natl Acad Sci U S A* 2013;110:9776–81.
- Duffy MJ, Mullooly M, O'Donovan N, Sukor S, Crown J, Pierce A, et al. The ADAMs family of proteases: new biomarkers and therapeutic targets for cancer? *Clin Proteomics* 2011;8:9.
- Fuchs BC, Hoshida Y, Fujii T, Wei L, Yamada S, Lauwers GY, et al. Epidermal growth factor receptor inhibition attenuates liver fibrosis and development of hepatocellular carcinoma. *Hepatology* 2014;59:1577–90.
- Chen J, Chen JK, Nagai K, Plieth D, Tan M, Lee TC, et al. EGFR signaling promotes TGF β -dependent renal fibrosis. *J Am Soc Nephrol* 2012;23:215–24.
- Kefaloyianni E, Muthu ML, Kaeppler J, Sun X, Sabbisetti V, Chalaris A, et al. ADAM17 substrate release in proximal tubule drives kidney fibrosis. *JCI Insight* 2016;1:e87023. doi:10.1172/jci.insight.87023
- Zhou Y, Lee JY, Lee CM, Cho WK, Kang MJ, Koff JL, et al. Amphiregulin, an epidermal growth factor receptor ligand, plays an essential role in the pathogenesis of transforming growth factor- β -induced pulmonary fibrosis. *J Biol Chem* 2012;287:41991–2000.
- Shostak K, Chariot A. EGFR and NF- κ B: partners in cancer. *Trends Mol Med* 2015;21:385–93.
- Lichtenberger BM, Gerber PA, Holcman M, Buhren BA, Amberg N, Smolle V, et al. Epidermal EGFR controls cutaneous host defense and prevents inflammation. *Sci Transl Med* 2013;5:199ra11–ra11.
- Hartmann M, Herrlich A, Herrlich P. Who decides when to cleave an ectodomain? *Trends Biochem Sci* 2013;38:111–20.
- Ferrini S, Rossello A, Nuti E, Fabbri M. Targeting ADAM17 sheddase activity in cancer. *Curr Drug Targets* 2016;17:1908–27.
- Le Gall SM, Maretzky T, Issuree PD, Niu XD, Reiss K, Saftig P, et al. ADAM17 is regulated by a rapid and reversible mechanism that controls access to its catalytic site. *J Cell Sci* 2010;123:3913–22.
- Friedman S, Levy R, Garrett W, Doval D, Bondarde S, Sahoo T, et al. Clinical benefit of INCB7839, a potent and selective inhibitor of ADAM10 and ADAM17, in combination with trastuzumab in metastatic HER2 positive breast cancer patients. *Cancer Res* 2010;69(24 Supplement):5056.
- Zhu AX, Rosmorduc O, Evans TR, Ross PJ, Santoro A, Carrilho FJ, et al. SEARCH: a phase III, randomized, double-blind, placebo-controlled trial of sorafenib plus erlotinib in patients with advanced hepatocellular carcinoma. *J Clin Oncol* 2015;33:559–66.
- Sequist LV, Waltman BA, Dias-Santagata D, Digumarthy S, Turke AB, Fidias P, et al. Genotypic and histological evolution of lung cancers acquiring resistance to EGFR inhibitors. *Sci Transl Med* 2011;3:75ra26.
- Hobor S, Van Emburgh BO, Crowley E, Misale S, Di Nicolantonio F, Bardelli A. TGF α and amphiregulin paracrine network promotes resistance to EGFR blockade in colorectal cancer cells. *Clin Cancer Res* 2014;20:6429–38.
- Troiani T, Martinelli E, Napolitano S, Vitagliano D, Ciuffreda LP, Costantino S, et al. Increased TGF- α as a mechanism of acquired resistance to the anti-EGFR inhibitor cetuximab through EGFR-MET interaction and activation of MET signaling in colon cancer cells. *Clin Cancer Res* 2013;19:6751–65.
- Minakata K, Takahashi F, Nara T, Hashimoto M, Tajima K, Murakami A, et al. Hypoxia induces gefitinib resistance in non-small-cell lung cancer with both mutant and wild-type epidermal growth factor receptors. *Cancer Sci* 2012;103:1946–54.
- Wilson TR, Fridlyand J, Yan Y, Penuel E, Burton L, Chan E, et al. Widespread potential for growth-factor-driven resistance to anticancer kinase inhibitors. *Nature* 2012;487:505–9.
- Tanizaki J, Okamoto I, Okabe T, Sakai K, Tanaka K, Hayashi H, et al. Activation of HER family signaling as a mechanism of acquired resistance to ALK inhibitors in EML4-ALK-positive non-small cell lung cancer. *Clin Cancer Res* 2012;18:6219–26.
- Sasaki T, Koivunen J, Ogino A, Yanagita M, Nikiforov S, Zheng W, et al. A novel ALK secondary mutation and EGFR signaling cause resistance to ALK kinase inhibitors. *Cancer Res* 2011;71:6051–60.
- Tani T, Yasuda H, Hamamoto J, Kuroda A, Arai D, Ishioka K, et al. Activation of EGFR bypass signaling by TGF α overexpression induces acquired resistance to alectinib in ALK-translocated lung cancer cells. *Mol Cancer Ther* 2016;15:162–71.
- Dang M, Dubbin K, D'Aiello A, Hartmann M, Lodish H, Herrlich A. Epidermal growth factor (EGF) ligand release by substrate-specific a disintegrin and metalloproteases (ADAMs) involves different protein kinase C (PKC) isoenzymes depending on the stimulus. *J Biol Chem* 2011;286:17704–13.
- Willems SH, Tape CJ, Stanley PL, Taylor NA, Mills IG, Neal DE, et al. Thiol isomerases negatively regulate the cellular shedding activity of ADAM17. *Biochem J* 2010;428:439–50.
- Stawikowska R, Cudic M, Giulianotti M, Houghten RA, Fields GB, Minond D. Activity of a disintegrin and metalloprotease 17 (ADAM17) is Regulated by its non-catalytic domains and secondary structure of its substrates. *J Biol Chem* 2013;288:22871–9.
- Xu P, Liu J, Sakaki-Yumoto M, Derynck R. TACE activation by MAPK-mediated regulation of cell surface dimerization and TIMP3 association. *Sci Signal* 2012;5:ra34.
- Chavaroche A, Cudic M, Giulianotti M, Houghten RA, Fields GB, Minond D. Glycosylation of a disintegrin and metalloprotease 17 affects its activity and inhibition. *Anal Biochem* 2013;449C:68–75.
- Xu P, Derynck R. Direct activation of TACE-mediated ectodomain shedding by p38 MAP kinase regulates EGF receptor-dependent cell proliferation. *Mol Cell* 2010;37:551–66.
- Díaz-Rodríguez E, Montero JC, Esparís-Ogando A, Yuste L, Pandiella A. Extracellular signal-regulated kinase phosphorylates tumor necrosis factor alpha-converting enzyme at threonine 735: a potential role in regulated shedding. *Mol Biol Cell* 2002;13:2031–44.
- Maney SK, McIlwain DR, Polz R, Pandya AA, Sundaram B, Wolff D, et al. Deletions in the cytoplasmic domain of iRhom1 and iRhom2 promote shedding of the TNF receptor by the protease ADAM17. *Sci Signal* 2015;8:ra109.
- Maretzky T, McIlwain DR, Issuree PD, Li X, Malapeira J, Amin S, et al. iRhom2 controls the substrate selectivity of stimulated ADAM17-dependent ectodomain shedding. *Proc Natl Acad Sci U S A* 2013;110:11433–8.
- Nakayama H, Fukuda S, Inoue H, Nishida-Fukuda H, Shirakata Y, Hashimoto K, et al. Cell surface annexins regulate ADAM-mediated ectodomain shedding of proamphiregulin. *Mol Biol Cell* 2012;23:1964–75.
- Tsukamoto H, Tanida S, Ozeki K, Ebi M, Mizoshita T, Shimura T, et al. Annexin A2 regulates A disintegrin and metalloproteinase 17-mediated ectodomain shedding of pro-tumor necrosis factor- α in monocytes and colon epithelial cells. *Inflamm Bowel Dis* 2013;19:1365–73.
- Düsterhöft S, Michalek M, Kordowski F, Oldefest M, Sommer A, Röseler J, et al. Extracellular juxtamembrane segment of ADAM17 interacts with membranes and is essential for its shedding activity. *Biochemistry* 2015;54:5791–801.

37. Düsterhöft S, Höbel K, Oldefest M, Lokau J, Waetzig GH, Chalaris A, et al. A disintegrin and metalloprotease 17 dynamic interaction sequence, the sweet tooth for the human interleukin 6 receptor. *J Biol Chem* 2014;289:16336–48.
38. Hartmann M, Parra LM, Ruschel A, Böhme S, Li Y, Morrison H, et al. Tumor suppressor NF2 blocks cellular migration by inhibiting ectodomain cleavage of CD44. *Mol Cancer Res* 2015;13:879–90.
39. Parra LM, Hartmann M, Schubach S, Li Y, Herrlich P, Herrlich A. Distinct ICD substrate modifications selectively regulate ectodomain cleavage of NRG1 or CD44. *Mol Cell Biol* 2015;35:3381–95.
40. Parra LM, Hartmann M, Schubach S, Ma J, Herrlich P, Herrlich A. Growth factor and co-receptor release by structural regulation of substrate metalloprotease accessibility. *Sci Rep* 2016;6:37464.
41. Razick S, Mora A, Michalickova K, Boddie P, Donaldson IM. iRefScape. A Cytoscape plug-in for visualization and data mining of protein interaction data from iRefIndex. *BMC Bioinformatics* 2011;12:388.
42. Villaveces JM, Jiménez RC, Porras P, Del-Toro N, Duesbury M, Dumousseau M, et al. Merging and scoring molecular interactions utilising existing community standards: tools, use-cases and a case study. *Database* 2015; pii: bau131. doi: 10.1093/database/bau131
43. Hornbeck PV, Chabra I, Kornhauser JM, Skrzypek E, Zhang B. PhosphoSite: A bioinformatics resource dedicated to physiological protein phosphorylation. *Proteomics* 2004;4:1551–61.
44. Li X, Wilmanns M, Thornton J, Köhn M. Elucidating human phosphatase-substrate networks. *Sci Signal* 2013;6:rs10.
45. Duan G, Li X, Köhn M. The human DEPhOsporylation database DEPOD: a 2015 update. *Nucleic Acids Res* 2015;43(Database issue):D531–5.
46. Tuncbag N, Gosline SJ, Kedaigle A, Soltis AR, Gitter A, Fraenkel E. Network-based interpretation of diverse high-throughput datasets through the omics integrator software package. *PLoS Comput Biol* 2016;12:e1004879.
47. Barretina J, Caponigro G, Stransky N, Venkatesan K, Margolin AA, Kim S, et al. The cancer cell line encyclopedia enables predictive modelling of anticancer drug sensitivity. *Nature* 2012;483:603–7.
48. Petryszak R, Keays M, Tang YA. Expression Atlas update—an integrated database of gene and protein expression in humans, animals and plants. *Nucleic Acids Res* 2016;44:D746–52.
49. Sabbisetti VS, Ito K, Wang C, Yang L, Mefferd SC, Bonventre JV. Novel assays for detection of urinary KIM-1 in mouse models of kidney injury. *Toxicol Sci* 2013;131:13–25.
50. Subramanian A, Tamayo P, Mootha VK, Mukherjee S, Ebert BL, Gillette MA, et al. Gene set enrichment analysis: a knowledge-based approach for interpreting genome-wide expression profiles. *Proc Natl Acad Sci U S A* 2005;102:15545–50.
51. Luo B, Cheung HW, Subramanian A, Sharifnia T, Okamoto M, Yang X, et al. Highly parallel identification of essential genes in cancer cells. *Proc Natl Acad Sci U S A* 2008;105:20380–5.
52. Rameseder J, Krismer K, Dayma Y, Ehrenberger T, Hwang MK, Airoidi EM, et al. A multivariate computational method to analyze high-content RNAi screening data. *J Biomol Screen* 2015;20:985–97.
53. Kampmann M, Bassik MC, Weissman JS. Integrated platform for genome-wide screening and construction of high-density genetic interaction maps in mammalian cells. *Proc Natl Acad Sci U S A* 2013;110:E2317–26.
54. Wilson JL, Hemann MT, Fraenkel E, Lauffenburger DA. Integrated network analyses for functional genomic studies in cancer. *Semin Cancer Biol* 2013;23:213–8.
55. Tuncbag N, Braunstein A, Pagnani A, Huang SS, Chayes J, Borgs C, et al. Simultaneous reconstruction of multiple signaling pathways via the prize-collecting steiner forest problem. *J Comput Biol* 2013;20:124–36.
56. Linding R, Jensen LJ, Pasculescu A, Olhovskiy M, Colwill K, Bork P, et al. NetworkKIN: a resource for exploring cellular phosphorylation networks. *Nucleic Acids Res* 2008;36:D695–9.
57. Su G, Kuchinsky A, Morris JH, States DJ, Meng F. GLay: community structure analysis of biological networks. *Bioinformatics* 2010;26:3135–7.
58. Todoric J, Antonucci L, Karin M. Targeting inflammation in cancer prevention and therapy. *Cancer Prev Res* 2016;9:895–905.
59. Gao J, Aksoy BA, Dogrusoz U, Dresdner G, Gross B, Sumer SO, et al. Integrative analysis of complex cancer genomics and clinical profiles using the cBioPortal. *Sci Signal* 2013;6:pl1.
60. Nottingham LK, Yan CH, Yang X, Si H, Coupar J, Bian Y, et al. Aberrant IKK α and IKK β cooperatively activate NF- κ B and induce EGFR/AP1 signaling to promote survival and migration of head and neck cancer. *Oncogene* 2014;33:1135–47.
61. de Mestier L, Lardière-Deguelte S, Volet J, Kianmanesh R, Bouché O. Recent insights in the therapeutic management of patients with gastric cancer. *Dig Liver Dis* 2016;48:984–94.
62. Wroblewski LE, Peek RM. Helicobacter pylori in gastric carcinogenesis: mechanisms. *Gastroenterol Clin North Am* 2013;42:285–98.
63. Allen CT, Conley B, Sunwoo JB, Van Waes C. CCR 20th anniversary commentary: preclinical study of proteasome inhibitor bortezomib in head and neck cancer. *Clin Cancer Res* 2015;21:942–3.
64. Allen C, Saigal K, Nottingham L, Arun P, Chen Z, Van Waes C. Bortezomib-induced apoptosis with limited clinical response is accompanied by inhibition of canonical but not alternative nuclear factor- κ B subunits in head and neck cancer. *Clin Cancer Res* 2008;14:4175–85.
65. Cossu F, Milani M, Grassi S, Malvezzi F, Corti A, Bolognesi M, et al. NF023 binding to XIAP-BIR1: searching drugs for regulation of the NF- κ B pathway. *Proteins* 2015;83:612–20.
66. Obexer P, Auserlechner MJ. X-linked inhibitor of apoptosis protein - a critical death resistance regulator and therapeutic target for personalized cancer therapy. *Front Oncol* 2014;4:197.
67. Kaur S, Wang F, Venkatraman M, Arsura M. X-linked inhibitor of apoptosis (XIAP) inhibits c-Jun N-terminal kinase 1 (JNK1) activation by transforming growth factor beta1 (TGF-beta1) through ubiquitin-mediated proteosomal degradation of the TGF-beta1-activated kinase 1 (TAK1). *J Biol Chem* 2005;280:38599–608.
68. Dombrowsky SL, Samsøe-Petersen J, Petersen CH, Instrell R, Hedegaard AM, Thomas L, et al. The sorting protein PACS-2 promotes ErbB signalling by regulating recycling of the metalloproteinase ADAM17. *Nat Commun* 2015;6:7518.

Molecular Cancer Research

Functional Genomics Approach Identifies Novel Signaling Regulators of TGF α Ectodomain Shedding

Jennifer L. Wilson, Eirini Kefaloyianni, Lauren Stopfer, et al.

Mol Cancer Res 2018;16:147-161. Published OnlineFirst October 10, 2017.

Updated version Access the most recent version of this article at:
doi:[10.1158/1541-7786.MCR-17-0140](https://doi.org/10.1158/1541-7786.MCR-17-0140)

Supplementary Material Access the most recent supplemental material at:
<http://mcr.aacrjournals.org/content/suppl/2017/10/10/1541-7786.MCR-17-0140.DC1>

Cited articles This article cites 68 articles, 33 of which you can access for free at:
<http://mcr.aacrjournals.org/content/16/1/147.full#ref-list-1>

E-mail alerts [Sign up to receive free email-alerts](#) related to this article or journal.

Reprints and Subscriptions To order reprints of this article or to subscribe to the journal, contact the AACR Publications Department at pubs@aacr.org.

Permissions To request permission to re-use all or part of this article, use this link
<http://mcr.aacrjournals.org/content/16/1/147>.
Click on "Request Permissions" which will take you to the Copyright Clearance Center's (CCC) Rightslink site.